General synthesis and definitive structural identification of MN₄C₄ (M = Ni, Fe, Co) single atom catalysts with tunable electrocatalytic activities

Huilong Fei[1#], Juncai Dong[2#], Yexin Feng[3], Christopher S. Allen[4], Chengzhang Wan[1], Boris Volosskiy[1], Mufan Li[1], Zipeng Zhao[5], Yiliu Wang[1], Hongtao Sun[1], Pengfei An[2], Wenxing Chen[6], Zhiying Guo[2], Chain Lee[1], Dongliang Chen[2], Imran Shakir[7], Tiandou Hu[2], Yadong Li[6], Angus I. Kirkland[4], Xiangfeng Duan[1,8,], Yu Huang[5,8,*]*

[1]Department of Chemistry and Biochemistry, University of California, Los Angeles, Los Angeles, California 90095, USA; [2]Beijing Synchrotron Radiation Facility, Institute of High Energy Physics, Chinese Academy of Sciences, Beijing 100049, China; [3]State Key Laboratory of Chemo/Biosensing and Chemometrics and School of Physics and Electronics, Hunan University, Changsha 410082, P. R. China; [4]Departments of Materials and Chemistry, University of Oxford, Parks Road, Oxford OX1 3PH, UK and Electron Physical Sciences Imaging Centre (ePSIC), Diamond Light Source Ltd, Didcot, Oxford, OX11 0DE; [5]Department of Materials Science and Engineering, University of California, Los Angeles, Los Angeles, California 90095, USA; [6]Departmentof Chemistry, Tsinghua University, Beijing 100084, P. R. China; [7]Sustainable Energy Technologies Centre, College of Engineering, King Saud University, Riyadh 11421, Kingdom of Saudi Arabia; [8]California NanoSystems Institute, University of California, Los Angeles, Los Angeles, California 90095, USA.

*Correspondence to: Email: yhuang@seas.ucla.edu, xduan@chem.ucla.edu

#These authors contributed equally to this work

Mono-dispersed transition metal atoms supported on solid substrates have recently emerged as an exciting class of single atom catalysts with the combined merits of both the homogeneous and heterogeneous catalysts, including high atom utilization efficiency, superior durability and excellent recyclability. Rational design and synthesis of single atom catalysts are of immense interest but have so far been plagued by the lack of a definitive structure-catalytic property correlation. The development of general synthetic strategy to mono-dispersed single atoms with systematically tunable active sites and the ability to identify the exact atomistic coordination configurations are both essential in addressing

such challenges. Here we report a general approach to a series of mono-dispersed atomic transition metals (*e.g.*, Fe, Co, Ni) embedded in nitrogen-doped graphene. The systematic X-ray absorption fine structure analyses and direct transmission electron microscopy imaging unambiguously reveal single metal atoms adopting an identical MN_4C_4 atomic structure in the two-dimensional graphene lattices. The unambiguous structure determination allows density functional theoretical calculation prediction of MN_4C_4 moieties as efficient oxygen evolution catalysts with the activities following the trend of Ni > Co > Fe, which is confirmed by the electrochemical studies. Particularly, the NiN_4C_4 catalyst exhibits excellent activity and stability with low overpotential and high turnover frequency. The determination and correlation of atomistic structure with the catalytic properties represents a critical step towards the rational design and synthesis of precious or nonprecious atomic catalysts with exceptional atom utilization efficiency and catalytic activities.

Efficient and cost-effective electrocatalysts play critical roles in energy conversion and storage[1-3]. Homogeneous and heterogeneous catalysts represent two parallel frontiers of electrocatalysts, each with their own merits and drawbacks[4,5]. Homogeneous catalysts are attractive for highly uniform active sites, tunable coordination environment and maximized atom utilization efficiency, but are limited by their relatively poor stability or recyclability. Heterogeneous catalysts are appealing for their high durability, excellent recyclability, and easy immobilization and integration with electrodes, but usually with rather low atom utilization efficiency due to the limited surface sites accessible to reactants. To this end, considerable efforts have been devoted to developing nanoscale heterogeneous catalysts that can increase the exposed surface atoms[3]. However, the inhomogeneity in the distribution of particle sizes and facets poses a serious challenge for controlling active sites and fundamental mechanistic studies[6,7]. In contrast, the homogeneous catalysts typically exhibit the well-defined atomic structure with tunable coordination environment that is essential for deciphering the catalytic reaction pathway and rational design of targeted catalysts with tailored catalytic properties[8].

Single atom catalysts (SACs) with mono-dispersed single atoms supported on solid substrates are recently emerging as an exciting class of catalysts that combine the merits of both homogeneous catalysts and heterogeneous catalysts[9-14]. However, most SACs studied to date

employ metal oxides (*e.g.*, TiO$_2$, CeO$_2$ and FeO$_x$) as supporting substrates to prevent atom aggregation[15-18], which cannot be readily applied in electrocatalytic applications due to their low electrical conductivity and/or poor stability in harsh liquid-phase electrolyte (*e.g.*, strong acid and base). Atomic transition metal-nitrogen moieties supported in nitrogen-doped carbon (M-N-Cs) represent a unique class of SACs with high electrical conductivity and superior (electro)chemical stability for electrocatalytic applications[19]. In particular, Fe-based M-N-Cs have been extensively studied as electrocatalysts towards oxygen reduction reaction (ORR) with the demonstrated activity and stability approaching those of commercial Pt/C catalysts[20,21]. In addition, as suggested by numerous theoretical studies, M-N-Cs are promising candidates for catalyzing a wide range of electrochemical processes, such as hydrogen reduction/oxidation reaction[22], CO$_2$/CO reduction[23], and N$_2$ reduction reactions[24].

A significant advantage of SACs is that the well-defined single atomic site could allow precise understanding of the catalytic reaction pathway, and rational design of the targeted catalysts with tailored catalytic activity (in a manner similar to the design and tailor of homogeneous catalysts). However, this perceived advantage was only investigated theoretically[23,24], but has not yet been demonstrated experimentally in M-N-Cs to date, largely because the existing M-N-Cs were generally obtained through pyrolysis of metal-, nitrogen- and carbon-containing molecular or polymeric precursors and the as-synthesized materials are typically highly heterogeneous, concurrently containing single atomic metals along with crystalline particles, crystalline and amorphous carbon[25-28]. Such structural and compositional heterogeneity poses a key obstacle to unambiguously identify the exact atomistic structure of the active sites and to further establish a definitive correlation with the catalytic properties that can guide the subsequent design of the future generations of SACs. This issue is readily manifested by tracking the research status of Fe-N-Cs ORR catalysts. Despite extensive efforts, the nature of the active sites and the atomistic structure of the FeN$_x$C$_x$ moieties remain elusive, largely due to the difficulty in synthesizing Fe-N-C catalysts free of Fe particles and the lack of accurate method to determine the coordination configuration of the metal sites[27,29]. Only until very recently that Zitolo *et al.* identified the porphyrin-based FeN$_4$C$_{12}$ moiety by X-ray absorption fine structure (XAFS) analysis[26]. Additionally, it is of great challenge to produce a series of closely related single atomic sites with systematically tunable compositions, which are essential for mechanistic studies. Although attempts have been made to elucidate the roles of different

metals in affecting the catalytic activity in M-N-Cs, they were severely complicated by the fact that the physicochemical characteristics (*e.g.*, the degree of graphitization, the carbon structure, the nitrogen doping types, surface area) of the synthesized M-N-Cs are highly dependent on the metal identity and any observed differences in catalytic activity are highly convoluted with various structural characteristics[30,31]. These limitations represent the key challenges in establishing the exact structure-to-property correlation in SACs, which is essential for the rational design and synthesis of new SACs with tailored activities for wide ranges of electrocatalytic processes[32-34].

Here we report a general approach to a series of atomic 3*d* metals embedded in nitrogen-doped holey graphene frameworks (M-NHGFs, M = Fe, Co or Ni), unambiguously determining their atomistic structures and their correlation with electrocatalytic activity towards oxygen evolution reaction (OER), a reaction that is essential for diverse clean energy technologies including water splitting, CO_2 reduction and rechargeable metal-air batteries[2,35-37]. Our studies show that different M-NHGFs adopt an identical MN_4C_4 moiety with the same local atomic coordination configuration embedded in graphene lattices, as revealed by thorough analyses of extended X-ray absorption fine structure (EXAFS) and X-ray absorption near-edge structure (XANES), and directly imaged by annular dark-field scanning transmission electron microscope (ADF-STEM). The unambiguous identification of the MN_4C_4 structural configuration has further allowed us to use density-functional theory (DFT) to explore the catalytic properties of M-NHGFs towards OER, which predicts that the catalytic activity and mechanistic pathways are strongly dependent on the *d*-orbital configurations of the metals with the activity trend Ni-NHGF > Co-NHGF > Fe-NHGF. This is further corroborated by electrochemical measurements, which show the Ni-NHGF exhibits outstanding catalytic activity, demonstrating the first example of single Ni atoms as highly efficient OER catalysts. Stability tests by electrochemical measurements and XAFS structural characterizations suggest that the Ni atoms and their coordinators in Ni-NHGF are able to withstand OER testing conditions and demonstrate good durability comparable to nanoparticle based catalysts.

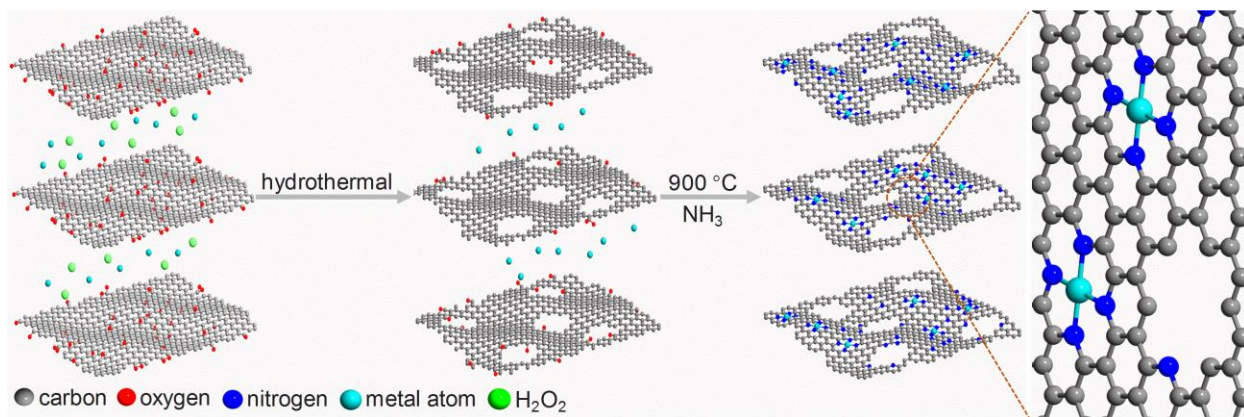**Synthesis and structural characterization of M-NHGFs**

Figure 1 │ Illustration of the preparation route to M-NHGFs. The graphene oxide solution with the presence of H_2O_2 and metal precursors was hydrothermally treated to form a 3D graphene hydrogel. After freeze-drying the hydrogel, a thermal annealing process in NH_3 atmosphere was used to further reduce the graphene and incorporate N-dopants into the two-dimensional graphene lattice.

The preparation of M-NHGFs involves a two-step process (Fig. 1). In brief, an aqueous suspension of graphene oxide (GO), metal precursor and H_2O_2 was prepared with proper ratio and hydrothermally treated to self-assemble into three-dimensional (3D) graphene hydrogel. After being freeze dried, the gel was then thermally annealed in NH_3 atmosphere to obtain M-NHGFs. This annealing treatment further reduces graphene and incorporates nitrogen dopants into the graphene lattice as the effective binding sites for individual metal atoms. In our synthetic strategy, the use of GO as carbon substrate precursor is advantageous in that it could be mass-produced and that its reduced form exhibits rich defective sites inherited from GO that provide tremendous numbers of vacancies for incorporating nitrogen atoms and anchoring metal atoms[38]. In addition, it can prevent the formation of amorphous carbon that has been proven to be a serious interfering species preventing clear atomistic imaging of the exact coordination configuration of the metal centers. The H_2O_2 added in the hydrothermal treatment was employed to create in-plane holes in graphene sheet via an oxidative-etching process, which is beneficial for mass transport during catalytic processes as demonstrated in our previous studies[39,40]. The increased porosity in M-NHGFs compared to its non-holey counterpart M-NGFs was characterized by scanning electron microscopy (SEM), transmission electron microscopy (TEM), and Brunauer–Emmett–Teller (BET) surface area analysis (Supplementary Figs 1-3). Compositional analysis by X-ray photoelectron spectroscopy (XPS) and inductively coupled plasma atomic emission spectroscopy (ICP-AES) reveals that the different M-NHGFs have similar contents of nitrogen (~5 at%) and metal (~0.05 at%) (Supplementary Fig. 4 and

Supplementary Table 1). It should be noted that keeping metal content at a sufficiently low level during preparation is critical in ensuring exclusive single atom dispersion as the increased loading could lead to aggregations and the formation of crystalline metal particles (Supplementary Figs 5 and 6) that could complicate the mechanistic studies.

Atomic structure analysis of M-NHGFs by XAFS and ADF-STEM

Element-selective XAFS spectroscopy including EXAFS and XANES is powerful in determining the coordination environment and chemical state of the absorbing center with high sensitivity. The existent forms of the metal in M-NHGFs (M = Fe, Co and Ni) are first identified by EXAFS analysis. Figure 2a shows the EXAFS Fourier transform (FT) of all three M-NHGFs. The Ni-NHGF exhibits a main peak at 1.44 Å, which is much shorter than the Ni-O peak at 1.65 Å for the NiO_6 octahedra in NiO reference and thus can be attributed to the backscattering between Ni and light atoms. In addition, the FT of Ni-NHGF also reveals a minor signal at 2.01 Å, which overlaps partially with the Ni-Ni peak at 2.18 Å for bulk Ni. The same observations can be made in Fe-NHGF and Co-NHGF with the minor peaks located at 2.03 and 1.92 Å, respectively, which are shifted to the lower R direction compared to the corresponding Fe-Fe (2.20 Å) and Co-Co (2.17 Å) peaks of bulk Fe and Co. We note that such EXAFS-FT profile, featured by the co-presence of the Gaussian-like main peak and the minor satellite peak, has never been observed in previously reported M-N-C materials[26,41], which turns out to be a key characteristic of the MN_xC_y atomic structure adopted by M-NHGFs and will be discussed later. EXAFS wavelet transform (WT) analysis is powerful in discriminating the backscattering atoms even when they overlap substantially in R-space, by providing not only radial distance resolution but also k-space resolution[42]. In contrast to the FT analysis, WT analysis of all M-NHGFs detects only one intensity maximum at *c.a.* 4.0 $Å^{-1}$ (Fig. 2b) that can be assigned to the M-N/O/C contributions (Supplementary Figs 7-9), suggesting that the metals in M-NHGFs exist as mononuclear M centers without the presence of metal-derived crystalline structures. FT and WT analysis of the control samples with higher metal loading reveals that the increased loading could lead to the formation of metallic crystallite (Supplementary Figs 7-11), which could prevent an unambiguous identification of atomic-site structure. Therefore, it is critical to keep the amounts of metal precursors sufficiently low to achieve exclusive atomic dispersion. While the pyrolysis of molecular or polymeric precursors used in the majority of previous studies require the inclusion of excessive amount of metals to catalyze the decomposition of molecular or polymeric

carbon precursors to form graphitized carbon with high electrical conductivity necessary for electro-catalytic applications, graphene oxide used in our synthetic strategy can be thermally reduced into conductive graphene without the catalytic effect from metals.
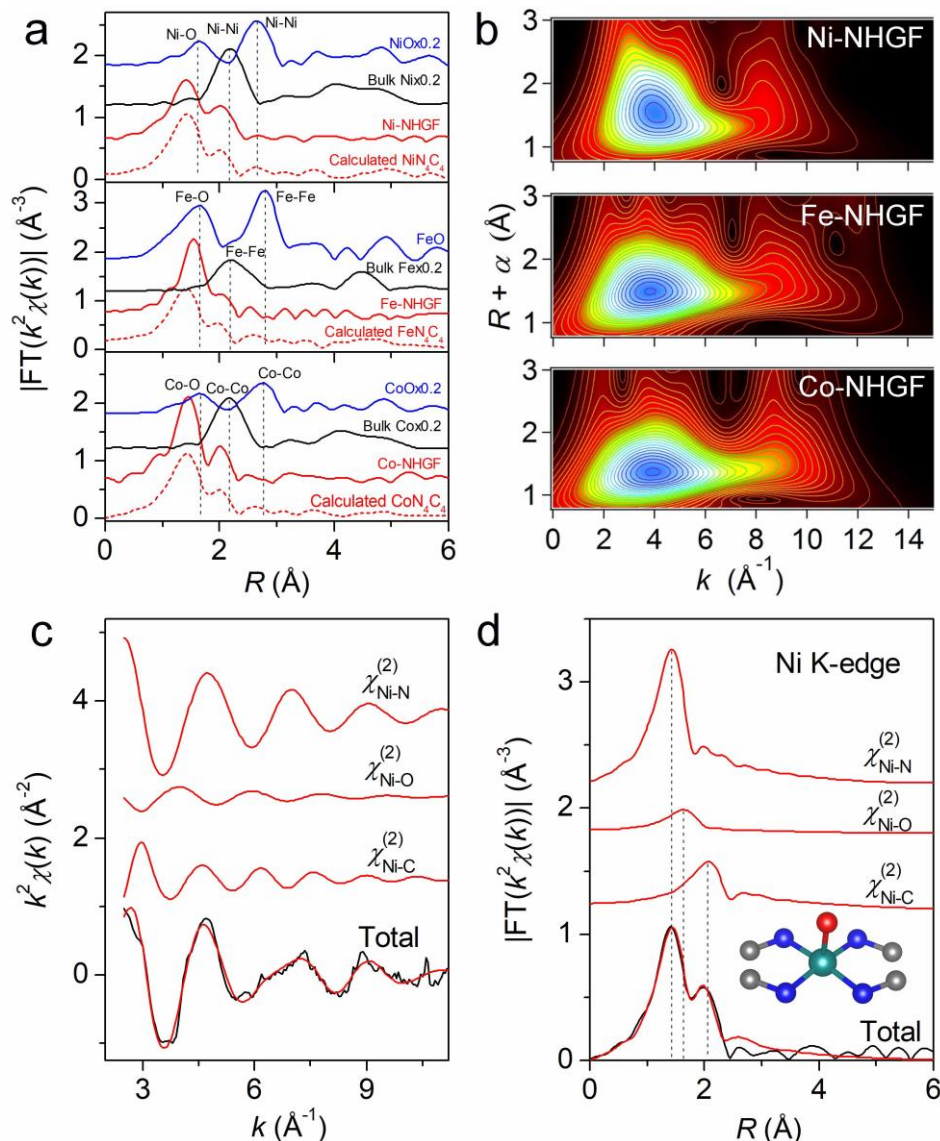

Figure 2 | Structural characterizations of M-NHGFs (M = Ni, Fe or Co) by EXAFS spectroscopy. a, Fourier transform magnitudes of the experimental K-edge EXAFS signals of M-NHGFs along with reference samples (solid lines). The dashed lines represent calculated spectra based on divacancy-based MN_4C_4 moiety enclosed in graphene lattice. The Fourier transforms are not corrected for phase shift. **b,** Wavelet transforms for the k^3-weighted EXAFS signals of M-NHGFs with optimum resolutions at 2.0 Å. The maxima at c.a. 4.0 Å^{-1} are associated with the M-N/O/C contributions. **c,d,** Ni K-edge EXAFS analysis of Ni-NHGF in k and R spaces, respectively. Curves from top to bottom are the Ni-N, Ni-O and Ni-C two-body backscattering signals $\chi^{(2)}$ included in the fit and the total signal (red line) superimposed on the experimental one (black line). The measured and calculated spectra show excellent agreement. The inset shows the structure of NiN_4C_4 moiety derived from EXAFS result, where the teal, red, blue and gray spheres represent Ni, O, N and C, respectively.

The coordination configurations for the MN_xC_y moieties in M-NHGFs were then investigated by quantitative least-squares EXAFS curve fitting analysis. The EXAFS spectrum of Ni-NHGF was first analyzed by using three backscattering paths, *i.e.*, Ni-N, Ni-O and Ni-C paths, based on the EXAFS-WT results. The best-fitting analyses show clearly that the main peak at 1.44 Å originates from Ni-N and Ni-O first shell coordination (Fig. 2c,d), whereas the minor satellite peak at 2.01 Å is satisfactorily interpreted by Ni-C contribution. The coordination numbers of the N and O atoms in the first coordination sphere of Ni are estimated to be 3.9 and 1.1 at distances of 1.89 and 2.10 Å, respectively (Supplementary Table 2), indicating a square-pyramidal configuration for the Ni-N/O bonding. Besides, a second coordination sphere by C atoms is clearly demonstrated at 2.65 Å with coordination number of 4.3 (Supplementary Table 2). Together, these analyses reveal a NiN_4C_4 moiety with one oxygen atom in the axial direction, as schematically shown in the inset of Fig. 2d. The same analysis was applied to Fe-NHGF and Co-NHGF, which are determined to adopt the identical coordination configurations as Ni-NHGF and the M-N, M-O and M-C distances are determined to be 1.98 Å, 2.16 Å and 2.67 Å, respectively, for Fe-NHGF, and 1.90 Å, 2.17 Å and 2.58 Å, respectively, for Co-NHGF (Supplementary Figs 12-16 and Supplementary Tables 3 and 4). We note that the as-determined M-N and M-O distances in our MN_4C_4 moiety agree well with those of the previously reported porphyrin-based FeN_4C_{12} moiety in Fe-N-C material[26] and the pyridinic-N-based CoN_4C_8 moiety in Co-N-C material[41], which were identified by EXAFS analysis and DFT predictions, whereas the M-C distance is considerably shorter than that (~ 3.00 Å) of the porphyrin-based FeN_4C_{12} moiety with the number of C atoms in the second coordination sphere larger than 10[26], but only slightly shorter than that (2.76 Å) of the pyridinic-N-based CoN_4C_8 moiety[41]. These comparisons exclude the existence of the porphyrin-based moiety in our MN_4C_4, but whether the pyridinic-N-based moiety are present in our MN_4C_4 moiety needs further examination.

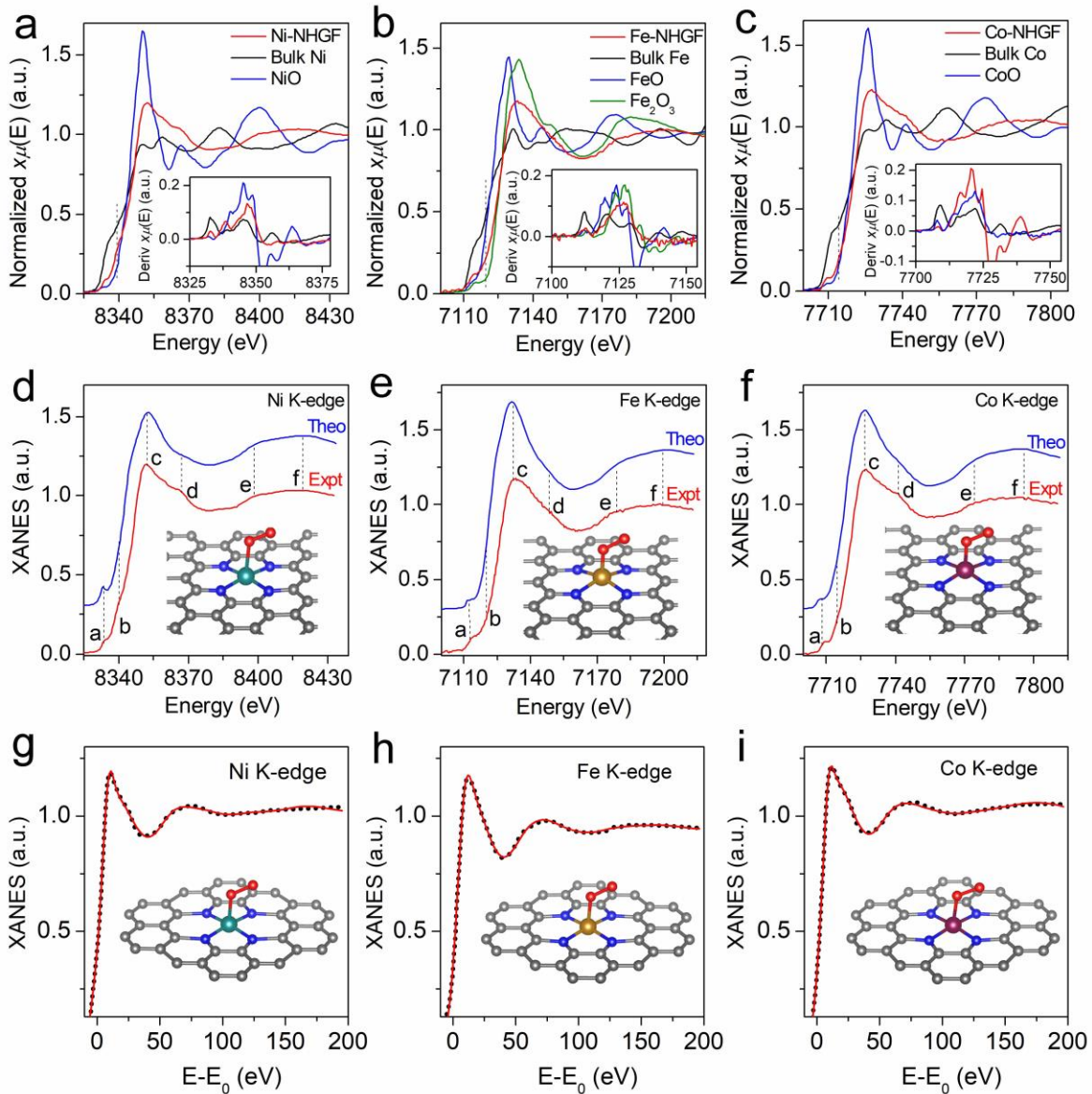**Figure 3 | Structural characterization by XANES spectroscopy on M-NHGFs (M = Ni, Fe or Co). a-c**, The experimental K-edge XANES spectra and first derivative curves (the inset) of M-NHGFs and reference samples. **d-f**, Comparison between the experimental K-edge XANES spectra of M-NHGFs and the theoretical spectra calculated based on MN_4C_4 moieties embedded in the 2D graphene lattice. The teal, golden and plum spheres symbolize Ni, Fe and Co, respectively, whereas the blue, red and grey spheres represent N, O and C, respectively. **g-h**, Comparison between the experimental XANES spectra (black dotted lines) for M-NHGFs and the best-fit theoretical spectra (solid red lines). The inset shows the geometrically refined MN_4C_4 structure.

XANES spectroscopy has higher sensitivity to the 3D arrangement of atoms around the photo-absorber and was applied to better identify the atomic-site structures. Figure 3a-c show the XANES profiles for Ni-NHGF, Fe-NHGF and Co-NHGF along with their corresponding reference samples, *i.e.*, bulk metal and metal oxide. The results show that for each metal the

XANES profile of M-NHGF is significantly different from those of the corresponding references. Interestingly, irrespective of the metals, the XANES profiles of all M-NHGFs are nearly identical, which strongly suggest the same coordination environment adopted by MN_4C_4 moieties in different M-NHGFs. Comparison of the first derivative XANES for Ni-NHGF, Fe-NHGF and Co-NHGF with references indicates that the stable valence states for the metals are c.a. +2, +3, and +2, respectively. Moreover, the pre-edge peak, which is due to a $1s$-$4p_z$ shakedown transition characteristic for a square-planar configuration with high D_{4h} symmetry, demonstrates rather weak intensity in all M-NHGFs, indicating a broken D_{4h} symmetry and calling for axial ligands.

We continued our path towards resolving the atomic-site structure in M-NHGFs by comparing simulated XANES spectra with the experimental spectra of various MN_xC_y moieties. To avoid artificial biases, all models were first optimized by DFT calculation. We have first evaluated previously identified porphyrin-based FeN_4C_{12} moiety[26] and pyridinic-N-based CoN_4C_8 moiety[41]. XANES calculation performed on the porphyrin-based MN_4C_{12} moieties, with various axial oxygen or nitrogen ligands considered (Supplementary Figs 17-19), show that all simulated spectra are drastically different from the experimental spectra after 50 eV above the absorption edge. Although with some improvement, the structures based on pyridinic-N-based MN_4C_8 architecture also show unsatisfactory agreement (Supplementary Figs 20-22).

We then carried out another series of XANES simulation by embedding the NiN_4C_4, FeN_4C_4 and CoN_4C_4 moieties in the two-dimensional graphene lattice (Supplementary Figs 23a, 24a and 25a). In contrast to the porphyrin-based moiety and the pyridinic-N-based moiety, the graphene-enclosed MN_4C_4 structure motif can be regarded as a single metal atom occupying the divacancy in the graphene lattice with coordination to four pyridinic N included in six-member rings. With such divacancy-based motif, the agreement is substantially improved over the entire energy range. Particularly, the white line and post-edge features in Ni-NHGF, Fe-NHGF and Co-NHGF are well reproduced, but a discrepancy is still present at the pre-edge features *a* and *b*. With the addition of one end-on dioxygen molecule to MN_4C_4 moieties in the axial position of the metal center, excellent agreement was obtained; all the features for the experimental spectra in Ni-NHGF, Fe-NHGF and Co-NHGF were correctly reproduced, especially for the weak pre-edge peaks *a-b* and the relative intensities between the peaks *c-f* (Fig. 3d-f). Further, it appears that the spectra are slightly influenced by the orientation of the absorbed dioxygen (six-member-

ring direction versus the five-member-ring direction) (Supplementary Figs 23b, 24b and 25b). However, when an additional N atom or end-on dioxygen was included, large discrepancies on the relative intensities between the pre-edge features and white line start to emerge (Supplementary Figs 23c-f, 24c-f, 25c-f). Together, these XANES simulations clearly demonstrate single metal centers with four N atoms and one adsorbed O atom in the first coordination sphere and four C atoms in the second coordination sphere (see the structure model in the inset of Fig. 3d-f), which is fully consistent with the EXAFS results. Structural refinement based on the as-determined MN_4C_4 moiety via XANES fitting reveals that the calculated spectra matches excellently with the experimental ones (Fig. 3g-i), and the bond metrics are in good agreement with those determined by EXAFS analysis and DFT prediction (Supplementary Table 5). Further, EXAFS simulations based on such divacancy-based MN_4C_4 moiety show the simulated EXAFS spectra are nearly identical to the experimental ones (Fig. 2a), and each coordination sphere's spectral contribution to the overall spectra can be well interpreted by the analysis of shell-by-shell EXAFS simulation (Supplementary Fig. 26). The combination of EXAFS-WT, EXAFS-FT and XANES analysis on Ni-NHGF, Fe-NHGF and Co-NHGF materials has unambiguously revealed the implantation of the NiN_4C_4, FeN_4C_4 and CoN_4C_4 moieties in the two-dimensional graphene lattices. Such divacancy-based MN_4C_4 moiety in graphene lattice is clearly distinct from previously identified porphyrin-based MN_4C_{12} moiety or the pyridinic-N-based MN_4C_8 moiety derived from pyrolysis of molecular or polymeric precursors. While this divacancy-based moiety has been previously explored theoretically for its intriguing electronic/magnetic/catalytic properties[43,44], its experimental identification has never been fully demonstrated, which seriously hampers its fundamental and applied investigations. We note that although several previous experimental studies suggested the divacancy-based MN_4C_4 moiety[12,45-47], there were insufficient spectroscopic evidences to date to verify its existence since such structural assignments were mainly based on EXAFS spectra and none of the previously reported EXAFS spectra could well match with the simulated standard spectrum of the divacancy-based MN_4C_4 moiety (see the comparison between our/others' experimental EXAFS spectra and the simulated standards in Supplementary Fig. 27). Significantly, our comprehensive structural analyses, for the first time, provide the solid spectroscopic fingerprints of this divacancy-based MN_4C_4 moiety. The formation of this MN_4C_4 moiety could be related to the use of crystalline graphene as the carbon precursor and the fact that it causes the least

geometrical distortion to the hosting graphene lattices by having the metal atom occupying the divacancy of graphene lattice. In contrast, the porphyrin-based FeN_4C_{12} moiety (and pyridinic-N-based MN_4C_8) cannot be easily integrated in graphene lattices[26].
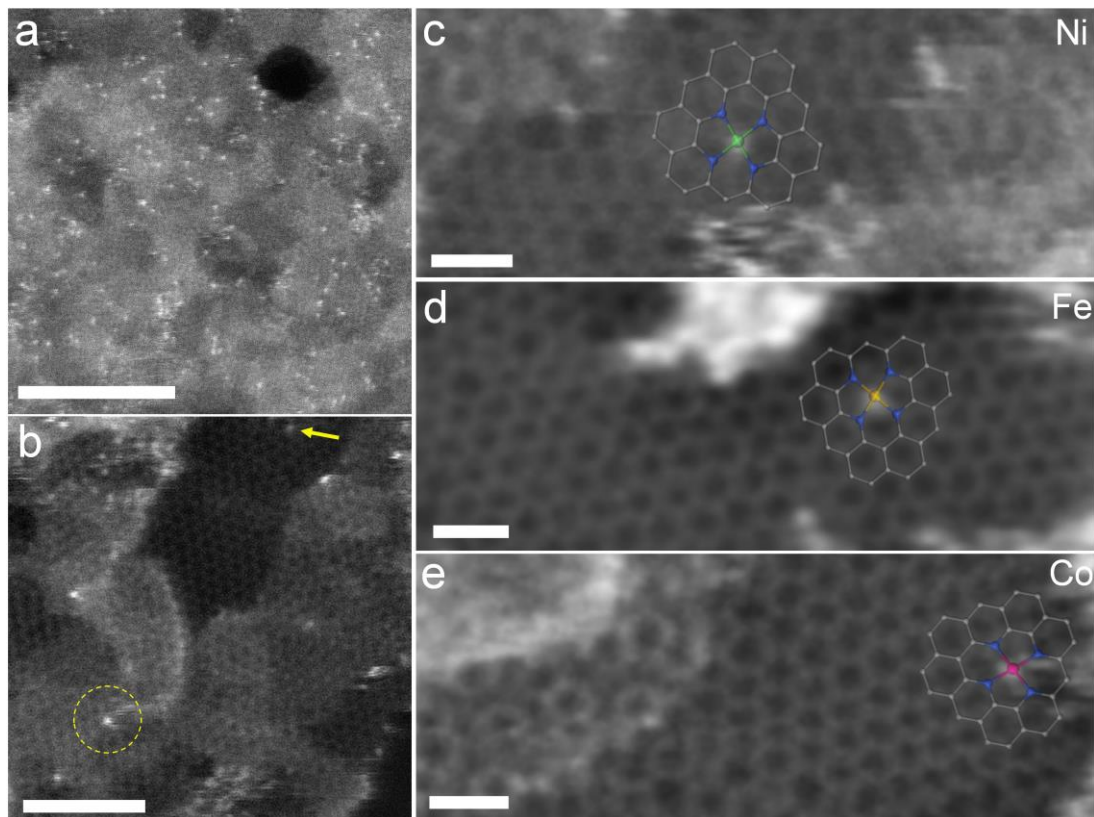

Figure 4 | Atomic structure characterizations of M-NHGFs by ADF-STEM. a,b, Uniform distribution of single metal atoms dispersed in the graphene matrix. The circle and arrow indicate some typical individual metal atoms in multi-layer and single-layer region of the graphene support, respectively. Scale bars correspond to 5 nm in (**a**) and 2 nm in (**b**). **c-e**, high resolution TEM images enable the direct visualization of the atomic metals of Ni (**c**), Fe (**d**) and Co (**e**) embedded in the 2D graphene lattice. The overlaid schematics represent the structural models determined from XAFS analysis. Scale bar, 0.5 nm. The bright region at the top part of Fig. 4d is attributed to out-of-focused thick graphene layers or non-planar flakes.

The atomic structures of M-NHGFs were further directly imaged by ADF-STEM performed on an aberration-corrected STEM at 80 keV. The STEM images show a uniform dispersion of the heavy metal atoms, almost exclusively in the single atom format as represented by the bright dots, throughout the graphene matrix (Fig. 4a,b). Though most of the metal atoms are identified in the region with multi-layer stacked graphene that prevents unambiguous resolution of the atomic structure, there are cases where they can be found in single-layer regions. The atomic thickness of single-layer graphene provides an ideal imaging platform for visualizing structural

details at atomic scale. As demonstrated in the high resolution STEM images (Fig. 4c-e), the atomic structures within the single-layer graphene can be clearly resolved and the observed coordination configurations of the atomic metals apparently match well with the MN_4C_4 moieties derived from XAFS studies. In addition, the arrangement of the light elements near the metal site and the overall graphene honeycomb lattice structure remain largely undistorted, which further excludes the existence of the porphyrinic structure or pyridinic-N-based structure in M-NHGFs since they can only form in strongly disordered graphene lattice or between graphene zigzag edges[26,41].

Theoretical and experimental evaluation on oxygen evolution catalysis

While Fe-, Co- and Ni-based oxides and derivatives are intensively studied as OER catalysts, the size dependence of electronic structure and catalytic reactivity suggests that the atomic metals within M-NHGFs could have different catalytic behavior[48]. In addition, the catalytic properties of SACs can be tuned by a ligand-field effect, which differs depending on the identity of the metal centers and their interaction with the coordination configuration. The well-defined atomistic structure and the adoption of the identical MN_4C_4 moiety by different metals provide us an ideal model system to probe the effects of the metal centers in determining the catalytic activity (both theoretically and experimentally). To this end, density functional theory (DFT) calculations using the Vienna *ab initio* Simulation Package (VASP)[49,50] were conducted to explore M-NHGFs as potential OER catalysts. Considering that the different M-NHGFs adopt identical atomic structure, DFT simulations are focused on elucidating the roles of metals in influencing the electronic nature of the atomic sites and consequently the energetics of OER. Consistent with prior studies[51], we assumed a four-step OER mechanism that proceeds through the OH*, O*, OOH* and O_2* (the asterisk denotes the adsorption site). As suggested by previous DFT calculations by us and others[52-54], the C close to N in nitrogen-doped carbon catalysts are the preferential binding sites for the oxygen intermediates rather than the N itself due to the doping-induced charge redistribution. Therefore, we considered both the M and C in MN_4C_4 moieties as possible absorption sites for the above-mentioned intermediates. For each intermediate, the preferred absorption location (M or C) can be determined by the difference in absorption energy between these two sites (see Supplementary Table 6). It can be concluded that whether the C atoms participate in the OER process depends strongly on the number of d electrons (N_d) of the metal in MN_4C_4 moieties. Specifically, for Fe ($N_d = 6$) and Co ($N_d = 7$), all

intermediates bind stronger at the M site than the C site and therefore the reaction proceeds through the single-site mechanism (Fig. 5a). On the other hand, for the Ni ($N_d = 8$), O* and OH* prefer to reside at the C site, while the OOH* is favorably adsorbed on the M atom. This reaction pathway is referred as the dual-site mechanism (Fig. 5b). The calculated energy diagrams of the OER at 1.23 V for the different M-NHGFs following the suggested reaction pathways are presented in Fig. 5c. One important parameter that can be used to evaluate the catalytic activity is the limiting reaction barrier, which is determined from the free energy of the rate-determining step (RDS). For Fe-NHGF, the RDS is the oxidation of O* to OOH* with limiting barrier as large as 0.97 eV. In addition, the free energy of the intermediates for Fe-NHGF are most negative among all studied catalysts, suggesting that the chemical adsorption of the intermediates is very strong, leading to a high activation barrier for the reaction to proceed. For the Co-NHGF, the RDS is the oxidation of OH* to O* with much lower limiting barrier of 0.52 eV. The Ni-NHGF with dual-site mechanism shows the smallest limiting barrier of 0.42 eV, with the formation of OOH* as the RDS. The desorption of O_2* from the active site is the last step for OER and its energy barrier is largest for Fe-NHGF, followed by Co-NHGF and Ni-NHGF. For comparison, we also included the energy diagram of the Ni-NHGF with single-site mechanism, which gives significantly larger limiting barrier of 1.24 eV, highlighting the critical role of the C atoms in the graphene-enclosed MN_4C_4 in facilitating the OER kinetics of Ni-NHGF. The energy diagrams for these three different catalysts at their respective minimum potential where all steps become downhill are shown in Supplementary Fig. 28. Further, by correlating the overpotential and descriptor (difference between free energy of O* and OH*), a typical volcano plot was constructed, where the NiN_4C_4 (dual-site mechanism) was located at the peak position and thus identified as the most active OER catalyst (Supplementary Fig. 29). Additional calculations performed on the MN_4C_4 moieties with the presence of the axial dioxygen molecule show the activity trend keeps the same as Ni > Co > Fe (Supplementary Fig. 30). Our simulation results indicate that the catalytic activity and reaction pathways are strongly dependent on the metal identity in M-NHGFs.

We then proceeded to evaluate the OER catalytic activities of M-NHGFs by electrochemical measurements. The testing was performed in traditional three-electrode system in 1 M KOH electrolyte. Fig. 5d shows the polarization curves obtained from linear sweep voltammetry (LSV) for the different M-NHGFs along with metal-free NHGF, which is prepared

in the same manner but without the addition of metal precursors. Precious metal-based OER catalyst RuO_2/C was also included for reference purpose. The results show that the metal-free NHGF exhibit inferior OER activity and the overpotential at current density of 10 mA cm^{-2} (η_{10}) is as large as 494 mV. The addition of metals results in activity increase to different degrees with Ni > Co > Fe. Specifically, the Ni-NHGF catalyst shows an onset potential of 1.43 V (defined as the potential at 0.5 mA cm^{-2}) and its η_{10} is 331 mV, much smaller than those of Co-NHGF (402 mV) and Fe-NHGF (488 mV). This experimentally observed trend is consistent with the predicted trend from DFT simulations. Optimizations on the synthetic conditions reveal that the catalytic activity of Ni-NHGF is sensitive to the annealing temperature and the Ni concentration (Supplementary Figs 31 and 32). In addition, it was found that acid leaching treatment did not lead to a decrease in OER activity, confirming the absence of Ni nanocrystallines (Supplementary Fig. 33). The control experiments on the non-holey Ni-NGF suggest that the porous structure introduced by H_2O_2 etching leads to improved OER activity in Ni-NHGF, which can be attributed to the enhanced mass transport properties (Supplementary Fig. 34). To put it into context, the η_{10} value of Ni-NHGF is superior or comparable to most of the documented nanoparticulate Ni catalysts, such as Ni/NiO(OH) particles embedded in nitrogen functionalized carbon (390 mV)[55], nickel vanadium layered double hydroxide (NiV-LDH) (318 mV)[56], exfoliated NiCo-LDH (334 mV)[57], NiCoO$_x$ thin film (380 mV)[58], and nickel carbide on conductive carbon (Ni$_3$C/C) (316 mV)[59].
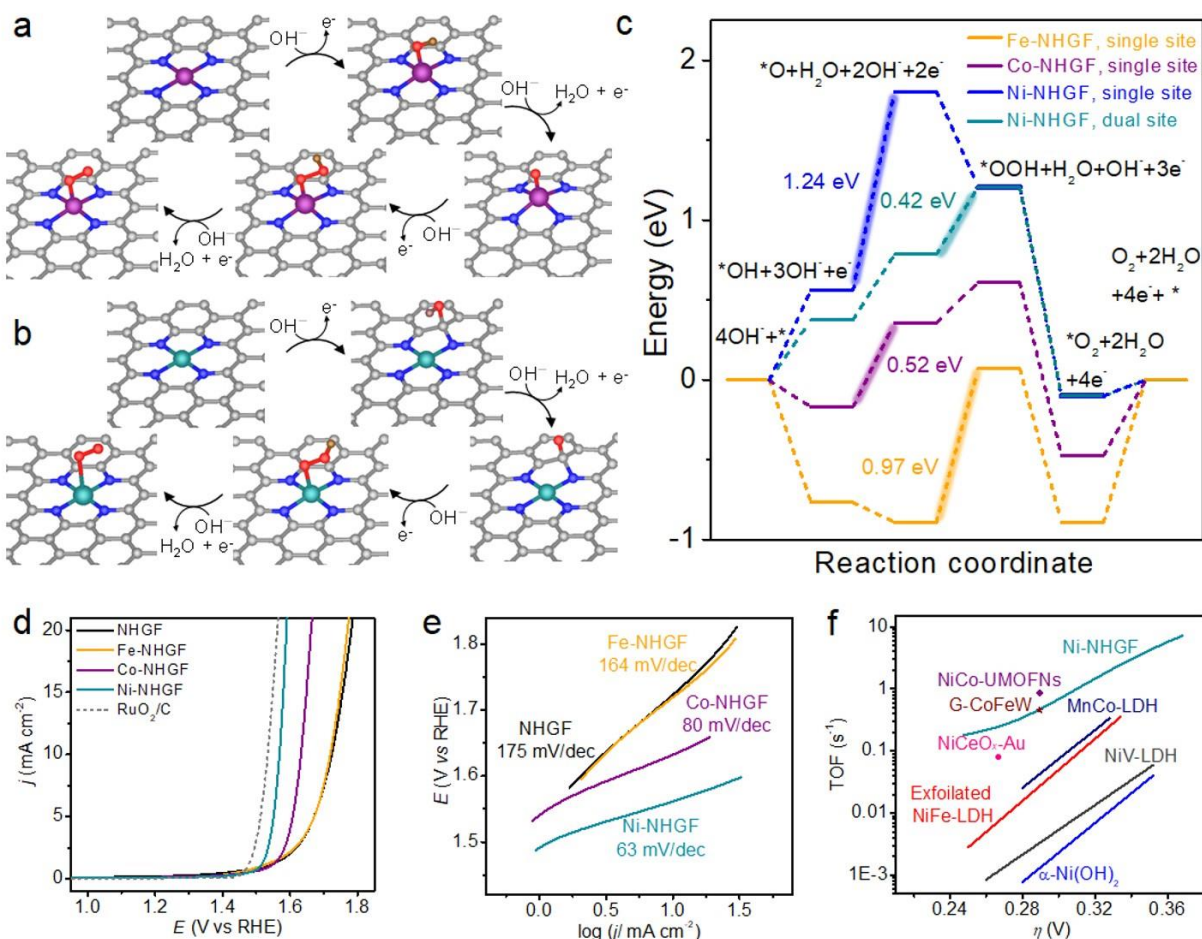
Figure 5 | Evaluation of catalytic activity by DFT simulations and electrochemical measurements. **a-b,** Proposed reaction scheme with the intermediates having optimized geometry of the single-site (**a**) and dual-site mechanism (**b**) towards OER. **c,** Free energy diagram at 1.23 V for OER over Fe-NHGF, Co-NHGF and Ni-NHGF with single-site mechanism, and Ni-NHGF with dual-site mechanism. The highlights indicate the rate-determine step with the values of the limiting energy barrier labeled. **d,** OER activity evaluated by LSV in 1 M KOH at the scan rate of 5 mV s^{-1} for NHGF, Fe-NHGF, Co-NHGF and Ni-NHGF along with RuO$_2$/C catalyst as reference point. The data is presented with iR-correction. **e,** The Tafel plots of the corresponding catalysts shown in (**d**). **f,** TOF values of the Ni-NHGF catalyst and other recently reported OER catalysts based on earth-abundant metals, including NiCo-UMOFNs (ref. 6), G-CoFeW (ref. 61), MnCo-LDH (ref. 63), NiCeO$_x$-Au (ref. 60), exfoliated NiFe-LDH (ref. 57), NiV-LDH (ref. 56), α-Ni(OH)$_2$ (ref. 62). The TOF values are based on the total amounts of metals for all catalysts.

The OER kinetics were then analyzed by Tafel plots (Fig. 5e). The Tafel slope for Ni-NHGF (63 mV decade^{-1}) is much smaller than Co-NHGF (80 mV decade^{-1}) and Fe-NHGF (164 mV decade^{-1}). The metal-free NHGF has an even larger Tafel slope of 175 mV decade^{-1}, suggesting the important roles of metals in promoting the reaction kinetics. The Faradaic efficiency of Ni-NHGF was determined to be ~99.2% by rotating ring-disk electrode (RRDE) technique (Supplementary Figs 35 and 36), indicating the exclusive generation of O$_2$ during OER

process through a 4-electron process, *i.e.*, $4\,OH^- \rightarrow O_2 + 2\,H_2O + 4\,e^-$. To evaluate the intrinsic activity of Ni-NHGF, we estimated the turnover frequency (TOF) that indicates the activity of a catalyst on the per-active-site basis. For the estimation, it is assumed all the Ni atoms participate in catalysis and one Ni atom contributes to one active site. The TOF of Ni-NHGF catalyst at different overpotentials is presented (Fig. 5f) along with the TOF values of some recently reported non-precious-metal catalysts, including gold-supported cerium-doped NiO_x (NiCeO$_x$-Au)[60], NiCo ultrathin metal–organic framework nanosheets (NiCo-UMOFNs)[6], gelled CoFeW oxyhydroxides (G-FeCoW)[61], nickel-vanadium monolayer double hydroxide (NiV-LDH)[56], nanostructured α-Ni(OH)$_2$[62], exfoliated NiFe-LDH[57], and MnCo-LDH[63]. The comparison results clearly show that Ni-NHGF is among the most active OER catalysts with the highest atom utilization efficiency. For example, at 0.3 V overpotential, the TOF of Ni-NHGF (0.72 s^{-1}) is two orders of magnitude higher than that of α-Ni(OH)$_2$ (0.0024 s^{-1}). Furthermore, this value is even higher than G-CoFeW (0.46 s^{-1})[61] and comparable to NiCo-UMOFNs (0.86 s^{-1})[6], which represent the most active OER catalysts reported to date.

Carbon is known to undergo oxidative degradation at high potentials and its electro-oxidation resistance is highly dependent on its exact physicochemical properties that can be tuned by functionalization (*e.g.*, heteroatom doping)[53,64]. The stability of Ni-NHGF was first evaluated by cyclic voltammetry scanning up to 2000 cycles and the cycled sample was characterized by XAFS. No significant activity degradation was observed after 2000 cycles (Supplementary Fig. 37a) and the XANES and EXAFS spectra of the cycled catalysts show essentially the same features as those of the fresh catalysts (Supplementary Fig. 37b,c), suggesting the metal atom center and its coordinating matrix are robust enough to withstand repeated electrochemical cycles with no significant Ni aggregation or apparent structural changes of the coordination environment, as further corroborated by the *in situ* XAFS studies on catalysts at *operando* states (Supplementary Fig. 38). Additional stability tests by galvanostatic measurements suggest that the Ni-NHGF can deliver stable activity up to 20 h at 10 mA cm^{-2} (Supplementary Fig. 39). Importantly, the electrochemical stability observed in Ni-NHGF is comparable to metal nanoparticles-based catalysts, which may be partly attributed to the highly active single metal sites that can facilitate efficient electron transfer for the desired water oxidation on the metal center so that the oxidative stress to carbon matrix can be effectively reduced. Lastly, we show that Ni-NHGF is also highly active towards ORR in alkaline media

(Supplementary Fig. 40) and therefore can serve as a superior bifunctional electrocatalyst (Supplementary Fig. 41 and Supplementary Table 7). To demonstrate its potential for practical applications, a two-electrode rechargeable Zn-air battery was fabricated from Ni-NHGF (Supplementary Fig. 42). Importantly, the device with Ni-NHGF catalyst air electrode show superior peak power density (158 mW cm^{-2}) when compared to that with precious Pt/C-RuO$_2$/C catalysts (98 mW cm^{-2}) (Supplementary Fig. 42b), which can be ascribed to its high catalytic activity as well as hierarchical porosity for improved mass transport.

Conclusions

In summary, we have developed a rational and general strategy to a series of mono-dispersed atomic metals embedded in nitrogen-doped graphene lattices. By combining EXAFS, XANES analyses with direct STEM imaging, we unambiguously identified that the resulting M-N-Cs (M = Fe, Co, Ni) adopt an identical MN$_4$C$_4$ configuration with single metal atom occupying the divacancies in graphene lattice that exerts the least distortion to the 2D graphene lattice. Significantly, the presence of the well-defined MN$_4$C$_4$ moieties in different M-NHGFs provides an ideal model system to probe and quantitatively establish the correlation between the atomistic structure of the metal centers and the catalytic properties, which, for example, successfully identified Ni-NHGF to be a highly active and stable OER catalyst, as demonstrated by both theoretical calculations and experimental studies. With the high intrinsic activity, the overall OER catalytic performance of Ni-NHGF may be further improved by increasing the metal loading and thus the density of active sites. Our study defines a general and efficient synthetic strategy to a broad class of MN$_4$C$_4$-based M-N-C catalysts for diverse electrocatalytic applications, including OER/ORR, hydrogen oxidation/evolution, CO$_2$ reduction and N$_2$ reduction.

Methods

Synthesis of M-NHGFs (M = Fe, Co, Ni). All chemicals were purchased from Sigma-Aldrich unless otherwise specified. Graphene oxide (GO) was synthesized by oxidation of natural graphite flakes (100 mesh) following a modified Hummers' method[65]. The M-NHGFs were synthesized using a two-step process. In a typical procedure for synthesizing Ni-NHGF, 50 µL of 3 mg mL^{-1} NiCl$_2$•6H$_2$O and 15 µL of 30% H$_2$O$_2$ were added into 10 mL of 2 mg mL^{-1} GO suspension and sonicated for 1 h. The mixed suspension was hydrothermally treated at 180 °C

for 6 h, forming a porous hydrogel. After being freeze-dried, the gel was placed in the center of 1-inch quartz tube furnace and annealed at 900 °C for 1 h with flows of Ar (100 sccm) and NH_3 (50 sccm) to obtain Ni-NHGF. As control samples, non-holey Ni-NGF was prepared without the addition of H_2O_2 during hydrothermal process and metal-free NHGF was prepared without the addition of Ni precursor. Fe-NHGF and Co-NHGF were prepared by using the same procedure but changing the metal precursor to 2 mg mL^{-1} $FeCl_3$ and 3 mg mL^{-1} $CoCl_2 \cdot 6H_2O$, respectively.

Material Characterizations. The morphology and structure of the resulting materials were characterized by scanning electron microscopy (SEM, Zeiss Supra 40VP), transmission electron microscopy (TEM, Titan S/TEM3 FEI), X-ray diffraction (XRD, Panalytical X'Pert Pro X-ray Powder Diffractometer) and X-ray photoelectron spectroscopy (XPS, Kratos AXIS Ultra DLD spectrometer). Quantitative analysis of metal loading was carried using inductively coupled plasma atomic emission spectroscopy (TJA RADIAL IRIS 1000 ICP-AES). The BET surface area and DFT pore size distribution were measured by Micromeritics ASAP 2020. Annular dark field scanning transmission electron microscopy (ADF STEM) imaging was performed on an aberration corrected JEOL ARM300CF STEM equipped with a JEOL ETA corrector operated at an accelerating voltage of 80 kV located in the electron Physical Sciences Imaging Centre (ePSIC) at Diamond Light Source. ADF imaging was performed at 80 keV with a CL aperture of 30 µm, convergence semiangle of 24.8 mrad, beam current of 12 pA, and acquisition angle of 27-110 mrad.

X-ray absorption data collection, analysis, and modeling. Fe, Co and Ni K-edge X-ray absorption spectra were acquired under ambient condition in fluorescence mode at beamlines 1W1B and 1W2B of Beijing Synchrotron Radiation Facility (BSRF), using a Si (111) double-crystal monochromator. The storage ring of BSRF was operated at 2.5 GeV with a maximum current of 250 mA in decay mode. While the energy was calibrated using Fe/Co/Ni foil, the incident and fluorescence x-ray intensities were monitored by using standard N_2-filled ion chambers and Ar-filled Lytle-type detector, respectively. A detuning of about 25% by misaligning the silicon crystals was performed to suppress the high harmonic content. The *in situ* XAFS experiments at operando state was performed using a house-made plastic electrochemical cell under the fluorescence model. The cell had flat walls (~ 4.5 cm wide) with a single circular hole of 0.8 cm in diameter. A thin carbon paper with thickness of 50 μm was loaded with Ni-NHGF catalysts and used as the working electrode, which was kept in contact with a slip of

copper tape and fixed with epoxy glue to the exterior of the wall of the cell, over the 0.8 cm hole, with the Ni-NHGF layer facing inward. A platinum spiral wire and a Hg/Hg_2Cl_2, KCl (saturated) electrode were used as counter electrode and reference electrode, respectively. During the measurement, a series of potentials controlled by an electrochemical workstation were applied to the working electrode in 1 M KOH solution. The XAFS raw data were background-subtracted, normalized, and Fourier transformed by the standard procedures with the ATHENA program[66,67]. Least-squares curve fitting analysis of the EXAFS $\chi(k)$ data was carried out using the ARTEMIS program[66], based on the EXAFS equation which expressed in terms of single and multiple-scattering expansion is

$$\chi(k) = S_0^2 \sum_{\Gamma} \frac{N_{\Gamma} \left| F_{eff}^{\Gamma}(\pi, k, R_{\Gamma}) \right|}{k R_{\Gamma}^2} \exp(-2R_{\Gamma}/\lambda(k) - 2k^2\sigma_{\Gamma}^2) \sin(2kR_{\Gamma} + \phi_{\Gamma}(k) + 2\delta_c(k)) \quad (1)$$

where $k = \sqrt{2m_e(E-E_0)}$ represents a scale conversion from the photo energy (E, eV) to the wave number (k, Å^{-1}) of the excited photoelectron as measured from absorption threshold E_0. The sums are over a series of equivalent scattering paths, Γ, which originate at the central absorption atoms, travelling to one or more of the neighboring atoms, and then back to the original central atoms. The equivalent scattering paths, with a degeneracy of N_{Γ}, are grouped according to the atomic number of the passed atoms and the total path length R_{Γ} of the photoelectron. The dependence of the EXAFS oscillatory structure on path length and energy is reflected by the $\sin(2kR_{\Gamma} + \phi_{\Gamma}(k) + 2\delta_c(k))$ term, where $\phi_{\Gamma}(k)$ is the effective scattering phase shift for path Γ. $F_{eff}^{\Gamma}(\pi, k, R_{\Gamma})$ denotes the effective scattering amplitude for path Γ. The amplitude decay due to inelastic scattering is captured by the exponential term $\exp(-2R_{\Gamma}/\lambda(k))$, where $\lambda(k)$ is the photoelectron mean free path. Additional broadening effect due to thermal and structural disorder in absorber-scatterer(s) path lengths is accounted for by the Debye-Waller term $\exp(-2k^2\sigma_{\Gamma}^2)$. S_0^2 is a many-body amplitude-reduction factor due to excitation in response to the creation of the core hole. In present work, while the scattering amplitudes and phase shifts for all paths as well as the photoelectron mean free path were theoretically calculated by ab-initio code FEFF9.0[68], the variable parameters that are determined by using the EXAFS equation to fit the experimental data are N_{Γ}, R_{Γ}, and σ_{Γ}^2. The S_0^2 parameter was determined in the fit of Fe/Co/Ni standards, and used as fixed value in the rest of the EXAFS models. All fits were performed in

the *R* space with *k*-weight of 2. The EXAFS *R*-factor (R_f) that measures the percentage misfit of the theory to the data was used to evaluate the goodness of the fit. The best-fit results are shown in Supplementary Figs 12-16, with the fitting parameter values listed in Supplementary Tables 2-4.
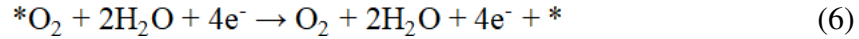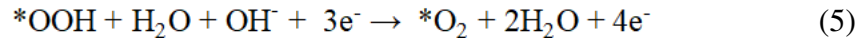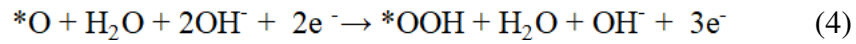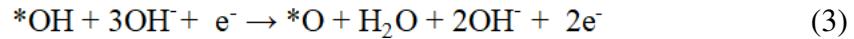
The Fe, Co and Ni K-edge theoretical XANES calculations were carried out with the FDMNES code in the framework of real-space full multiple-scattering (FMS) scheme using Muffin-tin (MT) approximation for the potential[68-70]. The energy dependent exchange-correlation potential was calculated in the real Hedin-Lundqvist scheme, and then the spectra are convoluted using a Lorentzian function with an energy-dependent width to account for the broadening due both to the core-hole width and to the final state width. The MN_xC_y (M = Fe, Co or Ni) moieties were built based on three typical architectures, namely the porphyrin-based and pyridinic-N-based ones, and those enclosed in a graphene sheet. The probability of various axial oxygen or nitrogen ligands was also considered in the calculation. Satisfactory convergence for the cluster sizes had been achieved. Additional EXAFS simulations based on the porphyrin-based moiety and divacancy-based MN_4C_4 moiety were performed with FEFF9.0, and the thermal disorder was taken into account by using the correlated Debye Model with Debye temperature of 475 K.

Quantitative XANES fitting was carried out with the MXAN code in the framework of the full MS scheme[71,72]. The potential calculation was consistent with FDMNES. Inelastic processes were taken into account by a convolution with a broadening Lorentzian function having an energy-dependent width of the form $\Gamma(E) = \Gamma_c + \Gamma_{mfp}(E)$ in which the constant part Γ_c takes care of both the core-hole lifetime and the experimental resolution, while the energy-dependent term represents intrinsic and extrinsic inelastic processes. The minimization of the M-NHGF XANES spectra has been carried out starting from the structures provided by DFT calculation. The fitting quality was evaluated using the square residue function (R_{sq}), where a statistical weight of 1 and a constant experimental error of 1.2% were used.

DFT modeling. The spin-polarized DFT calculations were performed by using the VASP. The Kohn-Sham wave functions were expanded in a plane wave basis set with a cutoff energy of 550 eV. The projector-augmented wave (PAW) method and PBE potential for the exchange-correlation functional were used. The Brillouin zone was sampled by the $3 \times 3 \times 1$ Monkshood-Pack k-point mesh. All atoms were allowed to relax until the forces are less than 0.01 eV/Å. We

employed a graphene supercell with surface periodicity of 6×6 including 72 atoms as a basis to construct the M-NHGFs moieties. A vacuum region of 15 Å was created to ensure negligible interaction between mirror images. The ZPE and entropy corrections were included by calculating the phonons by the using the Phonopy[73].

The overpotentials were evaluated using the approach developed by J. K. Nørskov[74]. The OER occur via the following steps:

$$4OH^- + * \rightarrow *OH + 3OH^- + e^- \tag{2}$$

$$*OH + 3OH^- + e^- \rightarrow *O + H_2O + 2OH^- + 2e^- \tag{3}$$

$$*O + H_2O + 2OH^- + 2e^- \rightarrow *OOH + H_2O + OH^- + 3e^- \tag{4}$$

$$*OOH + H_2O + OH^- + 3e^- \rightarrow *O_2 + 2H_2O + 4e^- \tag{5}$$

$$*O_2 + 2H_2O + 4e^- \rightarrow O_2 + 2H_2O + 4e^- + * \tag{6}$$

where * represents the preferable adsorption site for intermediates. For each step, the reaction free energy is calculated by

$$\Delta G = \Delta E + \Delta ZPE - T\Delta S + \Delta G_U + \Delta G_{pH} \tag{7}$$

where ΔE is the total energy difference between reactants and products of reactions, ΔZPE is the zero-point energy correction, ΔS is the vibrational entropy change at finite temperature T, $\Delta G_U = -eU$, where U is the electrode potential, ΔG_{pH} is the correction of the H^+ free energy.

The overpotential η can be evaluated from the Gibbs free energy differences of each step as

$$\eta = max[\Delta G_1, \Delta G_2, \Delta G_3, \Delta G_4, \Delta G_5]/e - 1.23] \tag{8}$$

where ΔG_1, ΔG_2, ΔG_3, ΔG_4 and ΔG_5 are the free energy of reaction (2)-(6).

Besides ZPE corrections and entropy corrections, we also take the influence of water environment into account by using a bilayer water model. The interaction between water and adsorbed intermediates will stabilize OH* and OOH* groups on the surfaces relative to adsorbed O atom, due to the hydrogen bonding[74].

In the main text, we have discussed two kinds of possible reaction pathways, depending on the favorite adsorption sites for O*, OH* and OOH* intermediate (center M atom or C atom adjacent to M-N$_4$ complex). The binding energies of O*, OH* and OOH* intermediates on the

two competing adsorption sites, for Fe-NHGF, Co-NHGF and Ni-NHGF systems are summarized in Supplementary Table 6. The binding energies of adsorbed intermediate I (I = O*, OH* or OOH*) are calculated by equation (9):

$$E_I^b = E_I - E_* - n \bullet \mu_H - m \bullet \mu_O \quad (9)$$

where E_I are the total energies of MN_4C_4-embedded graphene sheet with adsorbed intermediate I, E_* is the total energy of free MN_4C_4-embedded graphene sheet, n and m are the numbers of H and O atoms, μ_H and μ_O are chemical potentials of H and O, corresponding to gas phase molecules.

Electrochemical measurements. A CHI 760E electrochemical workstation (CH Instruments) was used to measure the electrocatalytic properties of the samples. The catalyst dispersion was prepared by mixing 4 mg catalyst, 1 mL ethanol and 40 µL 5 wt% Nafion solution and sonicating the mixture for 1 h. 14 µL of the catalyst suspension was drop-cast onto a freshly polished glassy carbon electrode (5 mm in diameter), leading to loading density of 0.275 mg cm^{-2}. For reference purpose, electrode of RuO_2/C catalyst, synthesized by oxidizing 20 wt% Ru/C (Premetek) in air at 300 °C for 1 h, was prepared with mass loading of 0.138 mg cm^{-2}. The electrochemical test was performed in three-electrode cell using Pt wire as counter electrode, Hg/HgO, 1 M NaOH as reference electrode. The measured potential against reference electrode was converted to reversible hydrogen electrode (RHE) according to $E_{RHE} = E_{Hg/HgO} + 0.915$ in 1 M KOH. For OER test, a 1 M KOH aqueous solution saturated with oxygen was used as the electrolyte. The LSV polarization curves were recorded at 5 mV s^{-1} after 5 sweeps to reach stable state. The Faradaic efficiency for OER was determined by rotating ring-disk electrode (RRDE) consisting of a glassy carbon disk electrode and a Pt ring electrode. Specifically, to determine the OER reaction pathway by detecting HO_2^- formation, the ring electrode is kept at a constant potential of 1.5 V vs RHE for oxidizing any HO_2^- produced at the disk electrode, which was swept at 10 mV s^{-1} in the OER potential region at a rotating speed of 1500 rpm. To determine the Faradaic efficiency, a constant current of 200 µA was applied to the disk electrode, and the ring electrode was held constant at 0.4 V vs RHE to reduce the O_2 generated at the disk. The Faradaic efficiency (f) is calculated by equation (10):

$$f = \frac{I_r}{I_d N} \quad (10)$$

where I_d and I_r are the disk and ring current, respectively, and N is the ring collection efficiency ($N \sim 0.2$, calibrated with a potassium ferricyanide redox couple).

The TOF value is calculated by equation (11):

$$\text{TOF} = \frac{j \times A}{4 \times F \times m} \quad (11)$$

where j is the current density at a given overpotential, A is the geometric surface area of the electrode, F is the Faraday constant, and m is the number of moles of metal on the electrode.

References

1. Faber, M. S. & Jin, S. Earth-abundant inorganic electrocatalysts and their nanostructures for energy conversion applications. *Energy Environ. Sci.* **7**, 3519-3542 (2014).
2. Jiao, Y., Zheng, Y., Jaroniec, M. & Qiao, S. Z. Design of electrocatalysts for oxygen- and hydrogen-involving energy conversion reactions. *Chem. Soc. Rev.* **44**, 2060-2086 (2015).
3. Seh, Z. W. *et al.* Combining theory and experiment in electrocatalysis: insights into materials design. *Science* **355**, eaad4998 (2017).
4. Astruc, D., Lu, F. & Aranzaes, J. R. Nanoparticles as recyclable catalysts: the frontier between homogeneous and heterogeneous catalysis. *Angew. Chem. Int. Ed.* **44**, 7852-7872 (2005).
5. Copéret, C., Chabanas, M., Petroff Saint-Arroman, R. & Basset, J.-M. Homogeneous and heterogeneous catalysis: bridging the gap through surface organometallic chemistry. *Angew. Chem. Int. Ed.* **42**, 156-181 (2003).
6. Zhao, S. *et al.* Ultrathin metal–organic framework nanosheets for electrocatalytic oxygen evolution. *Nat. Energy* **1**, 16184 (2016).
7. Ping, Y., Nielsen, R. J. & Goddard, W. A. The reaction mechanism with free energy barriers at constant potentials for the oxygen evolution reaction at the IrO_2 (110) surface. *J. Am. Chem. Soc.* **139**, 149-155 (2017).
8. Gorin, D. J., Sherry, B. D. & Toste, F. D. Ligand effects in homogeneous Au catalysis. *Chem. Rev.* **108**, 3351-3378 (2008).
9. Yang, X.-F. *et al.* Single-atom catalysts: a new frontier in heterogeneous catalysis. *Acc. Chem. Res.* **46**, 1740-1748 (2013).

10. Flytzani-Stephanopoulos, M. & Gates, B. C. Atomically dispersed supported metal catalysts. *Annu. Rev. Chem. Biomol. Eng.* **3**, 545-574 (2012).

11. Deng, D. *et al.* A single iron site confined in a graphene matrix for the catalytic oxidation of benzene at room temperature. *Sci. Adv.* **1**, e1500462 (2015).

12. Yin, P. *et al.* Single cobalt atoms with precise N-coordination as superior oxygen reduction reaction catalysts. *Angew. Chem. Int. Ed.* **55**, 10800-10805 (2016).

13. Liu, J. Catalysis by supported single metal atoms. *ACS Catal.* **7**, 34-59 (2017).

14. Zhang, W. & Zheng, W. Single atom excels as the smallest functional material. *Adv. Funct. Mater.* **26**, 2988-2993 (2016).

15. Lin, J. *et al.* Remarkable performance of Ir_1/FeO_x single-atom catalyst in water gas shift reaction. *J. Am. Chem. Soc.* **135**, 15314-15317 (2013).

16. Yang, M., Allard, L. F. & Flytzani-Stephanopoulos, M. Atomically dispersed Au–$(OH)_x$ species bound on titania catalyze the low-temperature water-gas shift reaction. *J. Am. Chem. Soc.* **135**, 3768-3771 (2013).

17. Jones, J. *et al.* Thermally stable single-atom platinum-on-ceria catalysts via atom trapping. *Science* **353**, 150-154 (2016).

18. Liu, P. *et al.* Photochemical route for synthesizing atomically dispersed palladium catalysts. *Science* **352**, 797-800 (2016).

19. Bezerra, C. W. B. *et al.* A review of Fe–N/C and Co–N/C catalysts for the oxygen reduction reaction. *Electrochim. Acta* **53**, 4937-4951 (2008).

20. Lefèvre, M., Proietti, E., Jaouen, F. & Dodelet, J.-P. Iron-based catalysts with improved oygen reduction activity in polymer electrolyte fuel cells. *Science* **324**, 71 (2009).

21. Wu, G., More, K. L., Johnston, C. M. & Zelenay, P. High-performance electrocatalysts for oxygen reduction derived from polyaniline, iron, and cobalt. *Science* **332**, 443 (2011).

22. Choi, W. I., Wood, B. C., Schwegler, E. & Ogitsu, T. Combinatorial search for high-activity hydrogen catalysts based on transition-metal-embedded graphitic carbons. *Adv. Energy Mater.* **5**, 1501423 (2015).

23. Tripkovic, V. *et al.* Electrochemical CO_2 and CO reduction on metal-functionalized porphyrin-like graphene. *J. Phys. Chem. C* **117**, 9187-9195 (2013).

24. Li, X.-F. *et al.* Conversion of dinitrogen to ammonia by FeN_3-embedded graphene. *J. Am. Chem. Soc.* **138**, 8706-8709 (2016).

25.	Kramm, U. I. *et al.* On an easy way to prepare metal–nitrogen doped carbon with exclusive presence of MeN$_4$-type sites active for the ORR. *J. Am. Chem. Soc.* **138**, 635-640 (2016).

26.	Zitolo, A. *et al.* Identification of catalytic sites for oxygen reduction in iron- and nitrogen-doped graphene materials. *Nat. Mater.* **14**, 937-942 (2015).

27.	Sahraie, N. R. *et al.* Quantifying the density and utilization of active sites in non-precious metal oxygen electroreduction catalysts. *Nat. Commun.* **6**, 8618 (2015).

28.	Holby, E. F. & Zelenay, P. Linking structure to function: the search for active sites in non-platinum group metal oxygen reduction reaction catalysts. *Nano Energy* **29**, 54-64 (2016).

29.	Sa, Y. J. *et al.* A general approach to preferential formation of active Fe–N$_x$ sites in Fe–N/C electrocatalysts for efficient oxygen reduction reaction. *J. Am. Chem. Soc.* **138**, 15046-15056 (2016).

30.	Peng, H. *et al.* Effect of transition metals on the structure and performance of the doped carbon catalysts derived from polyaniline and melamine for ORR application. *ACS Catal.* **4**, 3797-3805 (2014).

31.	Oh, H.-S. & Kim, H. The role of transition metals in non-precious nitrogen-modified carbon-based electrocatalysts for oxygen reduction reaction. *J. Power Sources* **212**, 220-225 (2012).

32.	Jiang, W.-J. *et al.* Understanding the high activity of Fe–N–C electrocatalysts in oxygen reduction: Fe/Fe$_3$C nanoparticles boost the activity of Fe–N$_x$. *J. Am. Chem. Soc.* **138**, 3570-3578 (2016).

33.	Jia, Q. *et al.* Spectroscopic insights into the nature of active sites in iron–nitrogen–carbon electrocatalysts for oxygen reduction in acid. *Nano Energy* **29**, 65-82 (2016).

34.	Fei, H. *et al.* Atomic cobalt on nitrogen-doped graphene for hydrogen generation. *Nat. Commun.* **6**, 8668 (2015).

35.	Cheng, F. & Chen, J. Metal-air batteries: from oxygen reduction electrochemistry to cathode catalysts. *Chem. Soc. Rev.* **41**, 2172-2192 (2012).

36.	Kim, W., McClure, B. A., Edri, E. & Frei, H. Coupling carbon dioxide reduction with water oxidation in nanoscale photocatalytic assemblies. *Chem. Soc. Rev.* **45**, 3221-3243 (2016).

37.   Gong, M. *et al.* An advanced Ni–Fe layered double hydroxide electrocatalyst for water oxidation. *J. Am. Chem. Soc.* **135**, 8452-8455 (2013).

38.   Lin, L.-C. & Grossman, J. C. Atomistic understandings of reduced graphene oxide as an ultrathin-film nanoporous membrane for separations. *Nat. Commun.* **6**, 8335 (2015).

39.   Xu, Y. *et al.* Holey graphene frameworks for highly efficient capacitive energy storage. *Nat. Commun.* **5**, 4554 (2014).

40.   Xu, Y. *et al.* Solution processable holey graphene oxide and its derived macrostructures for high-performance supercapacitors. *Nano Lett.* **15**, 4605-4610 (2015).

41.   Liu, W. *et al.* Single-atom dispersed Co-N-C catalyst: structure identification and performance for hydrogenative coupling of nitroarenes. *Chem. Sci.* **7**, 5758-5764 (2016).

42.   Funke, H., Scheinost, A. C. & Chukalina, M. Wavelet analysis of extended x-ray absorption fine structure data. *Phy. Rev. B* **71**, 094110 (2005).

43.   Kattel, S., Atanassov, P. & Kiefer, B. Stability, electronic and magnetic properties of in-plane defects in graphene: a first-principles study. *J. Phys. Chem. C* **116**, 8161-8166 (2012).

44.   Cheng, M.-J., Kwon, Y., Head-Gordon, M. & Bell, A. T. Tailoring metal-porphyrin-like active sites on graphene to improve the efficiency and selectivity of electrochemical CO_2 reduction. *J. Phys. Chem. C* **119**, 21345-21352 (2015).

45.   Cui, X. *et al.* A Graphene composite material with single cobalt active sites: a highly efficient counter electrode for dye-sensitized solar cells. *Angew. Chem. Int. Ed.* **55**, 6708-6712 (2016).

46.   Chen, Y. *et al.* Isolated single iron atoms anchored on N-doped porous carbon as an efficient electrocatalyst for the oxygen reduction reaction. *Angew. Chem. Int. Ed.* **56**, 6937-6941 (2017).

47.   Deng, D. *et al.* A single iron site confined in a graphene matrix for the catalytic oxidation of benzene at room temperature. *Sci. Adv.* **1**, e1500462 (2015).

48.   Tyo, E. C. & Vajda, S. Catalysis by clusters with precise numbers of atoms. *Nat. Nano.* **10**, 577-588 (2015).

49.   Kresse, G. & Hafner, J. *Ab initio* molecular dynamics for liquid metals. *Phy. Rev. B* **47**, 558-561 (1993).

50. Kresse, G. & Hafner, J. *Ab initio* molecular-dynamics simulation of the liquid-metal–amorphous-semiconductor transition in germanium. *Phy. Rev. B* **49**, 14251-14269 (1994).

51. Liao, P., Keith, J. A. & Carter, E. A. Water oxidation on pure and doped hematite (0001) surfaces: prediction of Co and Ni as effective dopants for electrocatalysis. *J. Am. Chem. Soc.* **134**, 13296-13309 (2012).

52. Feng, Y. *et al.* Tuning the catalytic property of nitrogen-doped graphene for cathode oxygen reduction reaction. *Phy. Rev. B* **85**, 155454 (2012).

53. Zhang, J., Zhao, Z., Xia, Z. & Dai, L. A metal-free bifunctional electrocatalyst for oxygen reduction and oxygen evolution reactions. *Nat. Nano.* **10**, 444-452 (2015).

54. Guo, D. *et al.* Active sites of nitrogen-doped carbon materials for oxygen reduction reaction clarified using model catalysts. *Science* **351**, 361-365 (2016).

55. Ren, J., Antonietti, M. & Fellinger, T.-P. Electrocatalysts: efficient water splitting using a simple Ni/N/C paper electrocatalyst. *Adv. Energy Mater.* **5**, 1401660 (2015).

56. Fan, K. *et al.* Nickel-vanadium monolayer double hydroxide for efficient electrochemical water oxidation. *Nat. Commun.* **7**, 11981 (2016).

57. Song, F. & Hu, X. Exfoliation of layered double hydroxides for enhanced oxygen evolution catalysis. *Nat. Commun.* **5**, 4477 (2014).

58. McCrory, C. C. L., Jung, S., Peters, J. C. & Jaramillo, T. F. Benchmarking heterogeneous electrocatalysts for the oxygen evolution reaction. *J. Am. Chem. Soc.* **135**, 16977-16987 (2013).

59. Xu, K. *et al.* Dual electrical-behavior regulation on electrocatalysts realizing eenhanced electrochemical water oxidation. *Adv. Mater.* **28**, 3326-3332 (2016).

60. Ng, J. W. D. *et al.* Gold-supported cerium-doped NiO_x catalysts for water oxidation. *Nat. Energy* **1**, 16053 (2016).

61. Zhang, B. *et al.* Homogeneously dispersed multimetal oxygen-evolving catalysts. *Science* **352**, 333-337 (2016).

62. Gao, M. *et al.* Efficient water oxidation using nanostructured α-nickel-hydroxide as an electrocatalyst. *J. Am. Chem. Soc.* **136**, 7077-7084 (2014).

63. Song, F. & Hu, X. Ultrathin cobalt–manganese layered double hydroxide is an efficient oxygen evolution catalyst. *J. Am. Chem. Soc.* **136**, 16481-16484 (2014).

64. Berenguer, R. *et al.* Enhanced electro-oxidation resistance of carbon electrodes induced by phosphorus surface groups. *Carbon* **95**, 681-689 (2015).

65. Hummers, W. S. & Offeman, R. E. Preparation of graphitic oxide. *J. Am. Chem. Soc.* **80**, 1339-1339 (1958).

66. Ravel, B. & Newville, M. ATHENA, ARTEMIS, HEPHAESTUS: data analysis for X-ray absorption spectroscopy using IFEFFIT. *J. Synchrotron Radiat.* **12**, 537-541 (2005).

67. Koningsberger, D. C. & Prins, R. Eds. *X-ray absorption: principles, applications, techniques of EXAFS, SEXAFS, and XANES*. **92**, *Wiley: New York* (1988).

68. Rehr, J. J. & Albers, R. C. Theoretical approaches to X-ray absorption fine structure. *Rev. Mod. Phys.* **72**, 621-654 (2000).

69. Joly, Y. X-ray absorption near-edge structure calculations beyond the muffin-tin approximation. *Phy. Rev. B* **63**, 125120 (2001).

70. Bunău, O. & Joly, Y. Self-consistent aspects of x-ray absorption calculations. *J. Phys.: Condens. Matter.* **21**, 345501 (2009).

71. Benfatto, M., Congiu-Castellano, A., Daniele, A. & Della Longa, S. MXAN : a new software procedure to perform geometrical fitting of experimental XANES spectra. *J. Synchrotron Radiat.* **8**, 267-269 (2001).

72. Hayakawa, K., Hatada, K., Longa, S. D., D'Angelo, P. & Benfatto, M. Progresses in the MXAN fitting procedure. *AIP Conf. Proc.* **882**, 111-113 (2007).

73. Togo, A., Oba, F. & Tanaka, I. First-principles calculations of the ferroelastic transition between rutile-type and $CaCl_2$-type SiO_2 at high pressures. *Phy. Rev. B* **78**, 134106 (2008).

74. Nørskov, J. K. *et al.* Origin of the overpotential for oxygen reduction at a fuel-cell cathode. *J. Phy. Chem. B* **108**, 17886-17892 (2004).

Author contributions

under the supervision of A.K. X.D., H.F., J.D., Y.F. and Y.H. co-wrote the paper. X.D. and Y.H. supervised the research. All authors discussed the results and commented on the manuscript.